Available online at www.sciencedirect.com
ScienceDirect
Acta Materialia 56 (2008) 5466–5476
Acta MATERIALIA
www.elsevier.com/locate/actamat

Dislocation dynamics simulations of plasticity in Fe laths at low temperature

Julien Chaussidon [a], Christian Robertson [b,*], David Rodney [a], Marc Fivel [a]

[a] SIMaP-GPM2, Grenoble INP, CNRS/UJF, 101 rue de la Physique, BP46, 38402 Saint Martin d'Hères cedex, France
[b] Service de Recherches Métallurgiques Appliquées, CEA/Saclay, Building 455, 91191 Gif-sur-Yvette, France

Received 25 April 2008; received in revised form 3 July 2008; accepted 19 July 2008
Available online 26 August 2008

Abstract

Plastic deformation in 16MND5 steel made of Fe laths is investigated using three-dimensional dislocation dynamics (DD) simulations, adapted to treat the body-centred cubic crystalline structure, strained in the ductile to brittle transition temperature range. In that regime, the edge segment velocity is proportional to the local effective resolved shear stress, whereas the screw segments follow a thermal activation scheme. The adopted cross-slip rules are derived from atomistic simulations, implemented in the DD code using a kinetic Monte Carlo algorithm. Specific loading and boundary conditions are worked out, with a view to accounting for the bainitic microstructure of the steel and its specific deformation mode. In these conditions, the implemented cross-slip behaviour is shown to play an essential role in the development of specific dislocation arrangements forming at different temperatures, also observed in 16MND5 steel. The presented results also provide insights on dislocation-based deformation mechanisms possibly involved in damage initiation.

Keywords: Bainitic steel; Dislocation dynamics; Microstructure; Dislocation mobility; Temperature effect

1. Introduction

16MND5 steel is used in the fabrication of nuclear reactor pressure vessels. In practice, the toughness behaviour of the steel is determined by testing macroscopic specimens at different temperatures, in the ductile to brittle transition temperature (DBTT) range [1–3]. The lower shelve behaviour observed during the tests is usually to initiation and propagation of cleavage cracks [2,3], following an initial ductile tearing stage [4]. 16MND5 steel is characterized by a refined microstructure made of blocks of parallel body-centred cubic (bcc) laths (1 μm thick platelets), obtained during an initial phase transformation [5,6]. Observations reveal that plastic strain in this material is markedly heterogeneous, i.e. it can sharply change from one lath block to another, even under homogeneous tensile loading conditions [7,8]. Prediction of damage thus needs a detailed, quantitative description of plastic strain development, at the scale of individual laths. In this work, intra-lath plasticity is investigated using three-dimensional dislocation dynamics (DD) methods, specially adapted to treat deformation of 16MND5 steel in the DBTT range.

In three-dimensional DD modelling, the material stress–strain behaviour is obtained from the multiplication and interaction of dislocation populations inside a simulation cell [9–12]. The discrete edge-screw DD model used here is adapted to the bcc crystalline structure, considering dislocation glide in the 12 $a/2\{110\}\langle 111\rangle$ slip systems. The edge dislocation mobility is proportional to the resolved shear stress, whereas the screw dislocation mobility follows a thermal activation theory [13–15]. In addition to these classical mobility rules, new procedures have been worked out in an attempt to treat some specific mechanisms acting in bainitic steel laths. These procedures are explained in details in Section 2, including a cross-slip algorithm that accounts for the twinning/anti-twinning asymmetry typical of bcc crystals, properties of the simulation volume,

* Corresponding author. Tel.:+33 1 69 08 22 70; fax: +33 1 69 08 71 67.
E-mail address: christian.robertson@cea.fr (C. Robertson).

1359-6454/$34.00 © 2008 Acta Materialia Inc. Published by Elsevier Ltd. All rights reserved.
doi:10.1016/j.actamat.2008.07.047

loading conditions and applied stress monitoring. Most of these developments are based on prior experimental observations [7,8], for which this paper is the numerical counterpart. In Section 3, the DD simulation results obtained at different temperatures are presented and discussed, including the dislocation density evolution and the analysis of the dislocation microstructure formation. The conclusions are presented in Section 4.

2. DD simulations adapted to the bcc structure

2.1. Dislocation mobility rules

The DD model used here adopts a discrete description of the dislocation lines, in the form of orthogonal edge and screw segments, as described in Ref. [16]. The absence of mixed segments is an intrinsic limitation of the DD code and could have a very important effect regarding junction formation. However; according to Ref. [7], junction pinning in 16MND5 steel deformed at low temperature is quite weak. Thus, this study will neglect this contribution and take full advantage of the simplicity offered by the edge-screw model. The edge segment velocity is proportional to the local effective resolved shear stress (see Fig. 1a). In bcc materials, screw dislocation mobility is due to the thermally activated formation of kink pairs [15]. At fixed temperature and plastic strain rate, the velocity of the screws can be modelled by a thermally activated law [13]:

$$v = v_D L \left(\frac{b}{l^*}\right)^2 \exp\left(\frac{\Delta G(\tau)}{K_B T}\right), \quad (1)$$

where v_D is the Debye frequency, L the dislocation length, l^* the critical kink pair length, K_B the Boltzmann constant and $\Delta G(\tau)$ the formation enthalpy of a single kink pair along a given screw line (entropy is neglected). The activation enthalpy as a function of the effective resolved shear stress is expressed, as proposed in Ref. [17]:

$$\Delta G(\tau) = \Delta H_v \left[1 - \left(\frac{\tau}{\tau_0}\right)^p\right]^q, \quad (2)$$

where ΔH_v is the activation energy at zero stress, τ_0 *is the Peierls stress and* τ is the applied resolved shear stress. The dimensionless parameters p and q ensure that Eq. (1) gives the correct yield stress, at a given temperature (see Fig. 1b). The activation parameters listed in Fig. 1b and used in Eqs. (1) and (2) are obtained from strain rate jump and temperature jump experiments, performed on 16MND5 steel specimens [18]. This procedure, explained in Ref. [15], assumes that:

$$\Delta H = -TV\left|\frac{d\tau}{dT}\right|_{\dot\gamma}, \quad (3)$$

where V is the activation volume, and $\left|\frac{d\tau}{dT}\right|_{\dot\gamma}$ is the stress jump due to an imposed temperature jump for an imposed, constant strain rate γ dot. The activation volume V is given by

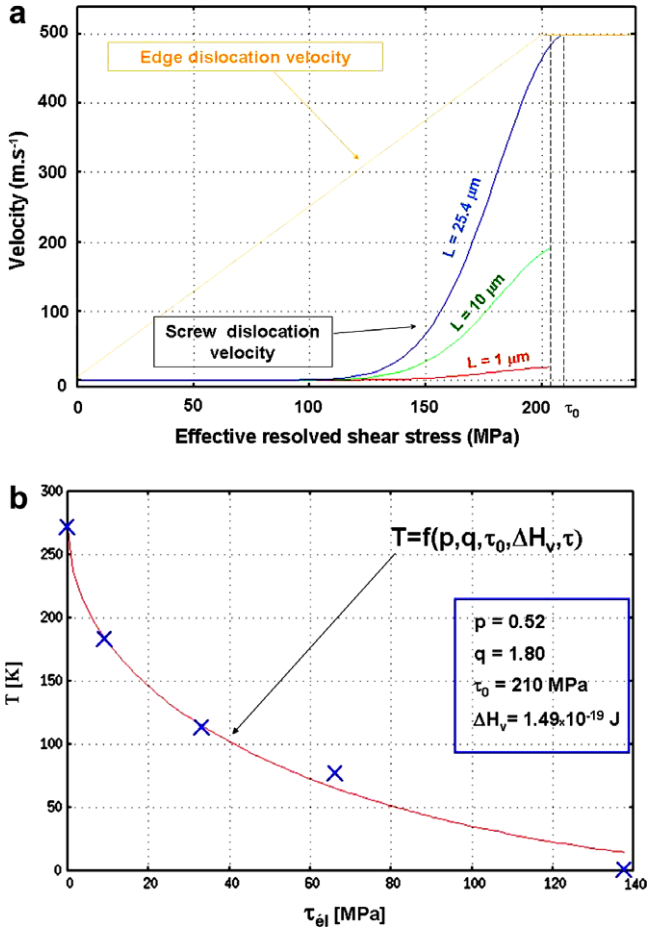

Fig. 1. Screw dislocation mobility rules. (a) The parameters ΔH_v, p and q fit the experimental evolution of the yield stress τ with temperature in 16MND5 steel. (b) Dislocation velocity at 200 K, from Eqs. (1) and (2), for three distinct screw lengths: 1, 10 and 25.4 μm. The edge velocity is proportional to the resolved shear stress and the saturation velocity is fixed to 500 m s^{-1}.

$$V = k_B T\left|\frac{\partial \ln(\dot\gamma/\dot\gamma_0)}{\partial\tau}\right|_T = k_B T\frac{\ln(\dot\gamma_2/\dot\gamma_1)}{\tau_2 - \tau_1}, \quad (4)$$

where $(\dot\gamma_2/\dot\gamma_1)$ is the strain rate ratio between temperature τ_1 and τ_2, where $(\tau_1 - \tau_2)$ corresponds to the magnitude of the imposed temperature jump.

These mobility rules induce strong mobility anisotropy between edge and screw segments, as depicted in Fig. 1a. For this reason, slip instability can take place whenever (fast-moving) edge segments generate long screw portions of the same sign, inside a small portion of the simulation volume. The repulsive forces between the screws thus become very large and produce unrealistically large displacements of the screws, per unit of time. Such unstable configurations can be avoided by decoupling the time scales for edge and screw segments. We left edge dislocations enough time to attain a stable position, before moving the screws again. In other words, stability is achieved by performing N "edge" time steps for each "screw" time step. The proper number N depends of the size of the simulation cell and on the applied plastic strain or stress rate:

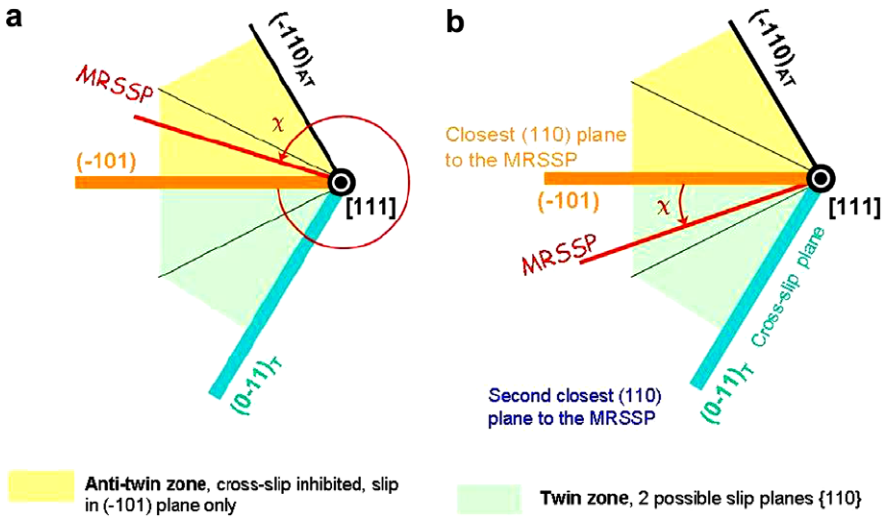

Fig. 2. Orientation of the MRSSP and cross-slip mechanism. (a) The MRSSP is located in a twin region: cross-slip is authorized towards the cross-slip plane; (b) the MRSSP is located in an anti-twin region: cross-slip is inhibited.

$N = 20$ in the present simulations. This procedure is physically justified by the fact that edge segments move much faster than screws and have thus always enough time to relax between two screw jumps.

2.2. Cross-slip algorithm

The following constitutive rules are developed in an attempt to account for the important cross-slip activity observed in deformed 16MND5 steel [7,8] and how it relates to the twinning/anti-twinning asymmetry of the bcc structure. The adopted rules are illustrated in the case of a [1 1 1] screw dislocation gliding in {1 1 0} planes (Fig. 2). Hence, dislocation glide in the {1 1 2} planes is not implemented in this DD model: up to 183 K, indeed, the dislocation structures analyzed after plastic deformation are consistent with a dominant dislocation activity in the {1 1 0} planes [7]. First, the maximum resolved shear stress plane (MRSSP) orientation, characterized by the angle χ with respect to the $(-1\,0\,1)$ plane taken as a reference, is determined (see Fig. 2a). The primary slip plane is then the closest {1 1 0} slip plane to the MRSSP. The cross-slip plane is defined as the second closest slip plane from the location of the MRSSP.

If the angle χ falls in an anti-twin zone (see Fig. 2a), cross-slip is inhibited and the screw dislocation glides in the primary slip plane only. This rule is based on prior molecular dynamics (MD) simulation results: nucleation of kink pairs never takes place in the anti-twin planes, regardless of the applied loading conditions [19,20]. If the angle χ falls in a twin zone, the screw dislocation can glide on either the primary or cross-slip planes (see Fig. 2b), depending on a cross-slip probability at each step to be presented below.

A realistic, averaged cross-slip probability computed in the DD framework has to be representative of numerous single cross-slip events, each one taking place at the atomic scale and during very short characteristic periods of time. In MD simulations for instance, the glide plane may change on the time scale of a few tens of picoseconds and at the length scale of one b, whereas in DD, the representative time and space scale are rather of the order of 1000 ps and 10 b. The required time and space scale averaging from MD to DD is achieved using the following kinetic algorithm.

Parameters p_1 and p_2 used hereafter correspond to the rates of gliding in slip plane 1 and slip plane 2 at the atomic scale. The average time before any of these two events takes place is:

$$\langle t \rangle = \frac{1}{p_1 + p_2}. \tag{5}$$

The average velocity on the plane 1 (respectively, on the plane 2) is $v_1 = p_1 d$ (respectively, $v_2 = p_2 d$) computed from Eq. (1), where d is the distance between two consecutive Peierls valleys. We then assume that the DD time step DT is much greater than $\langle t \rangle$ (DT$\gg\langle t \rangle$). During DT, the dislocation will thus undergo a number of atomic jumps equal to n:

$$n = \mathrm{DT} \cdot (p_1 + p_2). \tag{6}$$

The average velocity during DT is:

$$\langle v \rangle = \frac{n \cdot d}{\mathrm{DT}} = (p_1 + p_2) \cdot d = v_1 + v_2, \tag{7}$$

where v_1 and v_2 are the velocities[1] in the primary slip plane 1 and the cross-slip plane 2. In order to coarse-grain this process, at each time step DT, the glide plane of each screw segment is chosen according to the relative probability of

[1] In pure shear loading conditions, the resolved shear stresses in planes 1 and 2 are τ and $\tau.\cos(60°) = ½\ \tau$, respectively.

glide in slip plane 1 and 2. In this framework, the normalized probability P_1 to glide in the primary slip plane 1 is:

$$P_1 = \frac{p_1}{p_1 + p_2} = \frac{v_1}{v_1 + v_2}. \quad (8)$$

Similarly, the normalized probability P_2 to glide in the cross-slip plane 2 is:

$$P_2 = 1 - P_1 = \frac{v_2}{v_1 + v_2}. \quad (9)$$

In practice, v_1 (respectively, v_2) is computed for a given screw dislocation segment from the resolved shear stress on the primary slip plane (respectively, on the cross-slip plane) and Eq. (1). This velocity computation included the $\Delta G(\tau)$ expression (2) used with the experimental parameters listed on Fig. 1b. Then P_1 is calculated and compared to a random number P_{random}, between 0 and 1. If $P_1 < P_{\text{random}}$, then the dislocation continues in the primary slip plane; otherwise, it moves in the cross-slip plane. The angle Ψ corresponds to the average propagation direction with respect to the MRSSP. A large number of DD time steps are needed to obtain the same average glide direction as observed in MD at atomic scale. It is obtained by computing the projected dislocation velocities in the cross-slip plane over the projected dislocation velocity in the primary slip plane. Hence, by combining Eqs. (7)–(9), Ψ is given by:

$$\tan(\psi) = \frac{\frac{\sqrt{3}}{2} P_2 \langle v \rangle}{P_1 \langle v \rangle + P_2 \langle v \rangle} = \frac{\frac{\sqrt{3}}{2} v_2}{v_1 + \frac{1}{2} v_2} = \frac{\frac{\sqrt{3}}{2}}{\frac{v_1}{v_2} + \frac{1}{2}}. \quad (10)$$

If the glide occurs in an anti-twinnig zone, cross-slip is forbidden, $v_2 = 0$, and thus $\Psi = 0$. In the other case, i.e. when the dislocation glides in a twinning zone, it is possible to express $\tan(\Psi)$ as a function of χ by introducing Eq. (1) into Eq. (10):

$$\tan(\psi) = \frac{\frac{\sqrt{3}}{2}}{\exp[-\frac{\Delta G(\tau_1) + \Delta G(\tau_2)}{K_B T}] + \frac{1}{2}} = \frac{\frac{\sqrt{3}}{2}}{\exp[-\frac{\Delta G(\tau \cdot \cos\chi) + \Delta G(\tau \cdot \cos(60° - \chi))}{K_B T}] + \frac{1}{2}}, \quad (11)$$

where τ is the resolved shear stress on the MRSSP, τ_1 is the resolved shear stress on the primary slip plane and τ_2 is the resolved shear stress on the cross-slip plane.

From Eqs. (10) and (11), it is established that the cross-slip behaviour introduced here gives rise to a glide velocity asymmetry between tensile and compressive stresses (see Fig. 3a and b) due to the twinning/anti-twinning asymmetry, in agreement with experimental [21] and molecular static simulations results [19,22,23].

2.3. Simulation volume and initial dislocation microstructure

Transmission electron microscopy (TEM) examinations reveal that plastic strain in 16MND5 steel is quite heterogeneous and develops particularly into specific lath blocks, especially at low temperature [7]. These observations are consistent with polycrystalline plasticity models, accounting for the bainitic microstructure of the steel [24]. Deformation is indeed localized into high-strain bands corresponding to lath blocks having specific orientations with respect to the rest of the microstructure that undergo significant bending strains [24]. Existence of such a micro-bending mode is confirmed by scanning electron microscopy (SEM) observations of tensile specimens equipped with surface strain markers (micro-grids) [24]. This is also supported by TEM examinations, where intra-lath staining is visible in the form of tilt boundary arrangements [8]. Based on these experiments and models, it is believed that prediction of damage in 16MND5 steel needs a precise knowledge of plastic strain development, at the scale of individual laths. In this paper, all the three-dimensional DD simulation cells thus correspond to a $2 \times 10 \times 10\ \mu m^3$ single lath of bainite, as sketched in Fig. 4a.

In 16MDN5 steel, lath interfaces comprise regularly spaced screw dislocations with Burgers vectors aligned with both the lath plane and (in many cases) the lath growth direction. These structures are formed at the time of the initial Bainitic phase transformation [5,6,25,26] and constitute an important fraction of the initial dislocation sources, despite the presence of additional intra-lath dislocations. This assumption is consistent with the dislocation density evolution model developed in Ref. [8]: the initial interfacial dislocation density is sufficient to explain the observed strain-hardening rate at all temperatures (in the DBTT range). In the following, we thus assume that the initial dislocation microstructure is made of regularly spaced screw dislocations from slip systems $a/2[-1-11](101)$ and $a/2[-11-1](110)$, positioned in the simulated lath interfaces.[2] The initial dislocation density is fixed to $2 \times 10^{12}\ m^{-2}$, that is to say, one screw dislocation every 1 μm (see Fig. 4b). The $[-1-11]$ screw dislocations are parallel to the $(1-54)$ lath planes. The $[-11-1]$ dislocations are slightly tilted away (about 10°) from the (-154) lath planes.

The initial screw dislocations are introduced in a "virtual" simulation volume, surrounding the lath simulation volume (see Fig. 5a). These dislocations are pinned at their extremities and therefore operate as Frank–Read sources when the external load is applied: one part of the dislocation segments glides towards the lath volume while the other part glides towards the virtual volume (see Fig. 5b). This configuration (virtual + lath simulation volumes) ensures constant dislocation emission to accommodate the imposed strain, regardless of the initial dislocation source length. Dislocation segments located in the virtual region have special properties in order to avoid arbitrary changes in the lath region. Hence, the virtual segments are not present in the material: they are used to keep the connection between the segments of the initial interfacial sources, avoiding the use of artificial pinning points. For this reason, the stress field due to the virtual dislocations

[2] Other initial configurations have been tested, including a random distribution of sources from all the possible slip systems, yielding qualitative changes only.

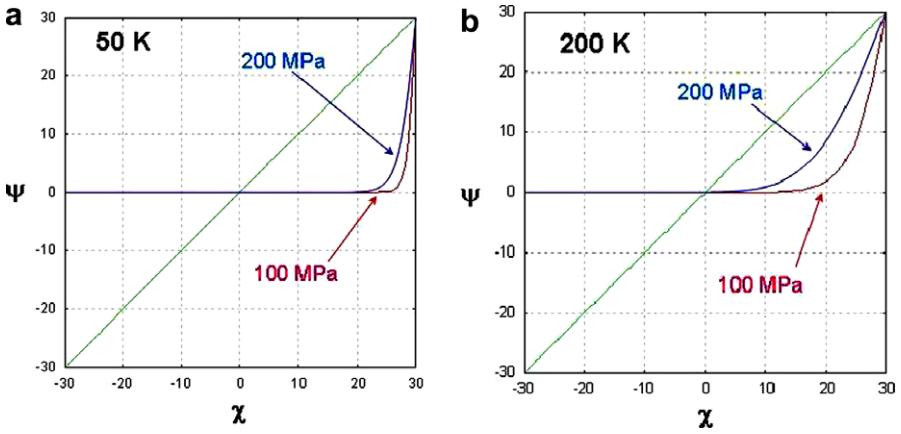

Fig. 3. Average propagation direction Ψ of a screw dislocation, as a function of the orientation χ of the MRSSP. Two distinct applied stress magnitudes are represented for each temperature: (a) 50 K and (b) 200 K.

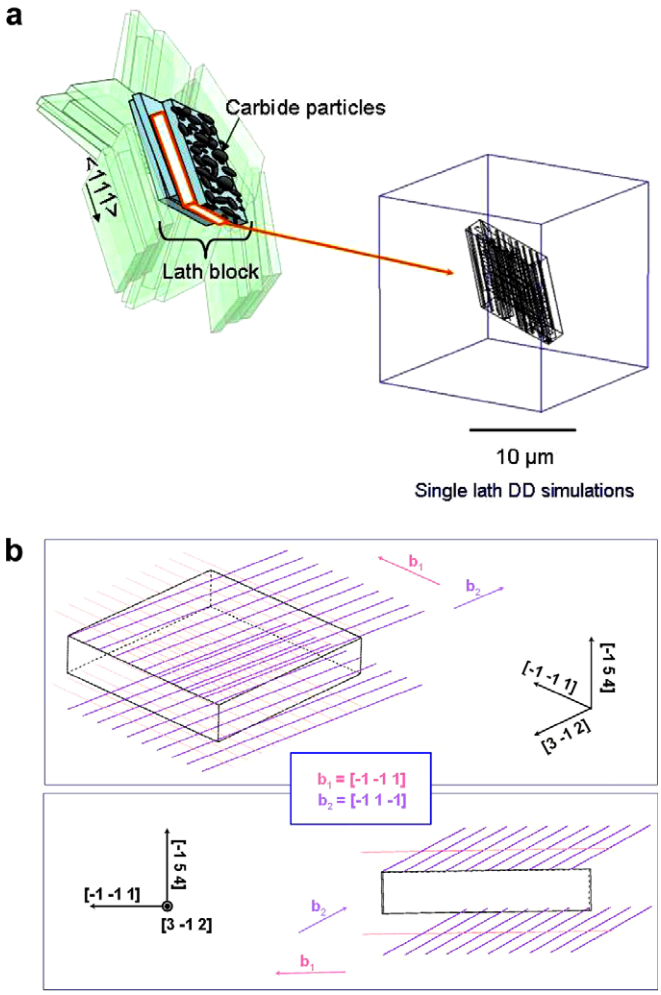

Fig. 4. Simulation volume geometry and initial dislocation microstructure. (a) The individual lath boundaries are decorated with a high density of carbide particles and lath blocks of different orientations. In the actual steel, this environment can produce a bending moment at the scale of individual laths. (b) The initial dislocation structure is placed near the simulation volume interfaces. The screw orientation b_1 is parallel to the $(-1\,5\,4)$ lath interfaces. The second screw orientation b_2 has the smallest possible disorientation with the $(-1\,5\,4)$ lath interfaces.

is not transmitted into the lath volume and cross-slip is forbidden in the virtual medium. Reversely, the internal stress induced by the bulk segments is not resolved on the virtual dislocations whose kinetics only depends on the applied loading stress. Prior TEM observations indicate that lath boundaries constitute a strong obstacle to dislocation motion, at least up to 8% macroscopic plastic strain [7,8]. For this reason, the simulated lath interfaces are made permeable in the virtual → lath direction and impermeable in the opposite lath → virtual direction (Fig. 5c).

2.4. Applied loading algorithm

The simulated lath is submitted to a simplified heterogeneous mechanical loading, intended to be representative of the experimentally observed micro-bending deformation mode. The applied stress field thus generates a bending moment about a single axis, parallel to the lath plane. The exact loading configuration relative to the lath geometry is sketched in Fig. 6.

The bending axis $\mathbf{e_2}$ is positioned at the middle of the lath and aligned parallel to the middle plane $(-1\,5\,4)$, where the applied stress cancels out. The selected traction/compression axis $\mathbf{e_1}$ is oriented at 45° with respect to the $[-1\,-1\,1]$ crystallographic direction. Therefore, the maximum resolved shear stress acts in the $a/2[-1\,-1\,1](1\,0\,1)$ slip system, referred to as the primary slip system. The second largest resolved shear stress acts in the $a/2[-1\,1\,-1](1\,1\,0)$ slip system, referred to as the secondary slip system. In the $(\mathbf{e_1},\mathbf{e_2},\mathbf{e_3})$ coordinate system shown in Fig. 6, the applied stress tensor is written:

$$\underline{\sigma}_{\text{app}} = \frac{h}{e}\begin{pmatrix} \sigma_{\text{app}}^{\text{ref}} & 0 & 0 \\ 0 & 0 & 0 \\ 0 & 0 & 0 \end{pmatrix}, \tag{12}$$

where h is the distance to the central (neutral) plane, e is the lath width and $\sigma_{\text{app}}^{\text{ref}}$ is a reference applied stress needed for load monitoring as explained below.

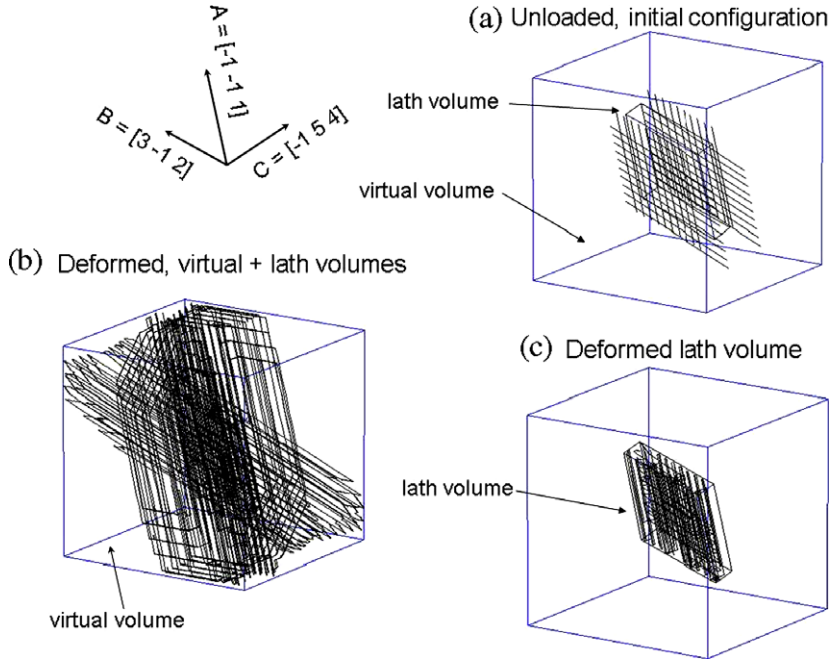

Fig. 5. DD simulation volume configuration accounting for the properties of interfacial dislocation sources. (i) Initial, unloaded dislocation structure; (ii) dislocation structures forming during plastic deformation, in the virtual and in the lath simulation volumes; (iii) only the dislocations present in the lath simulation volume are accounted for in the feedback control procedures and the analysis of plastic deformation.

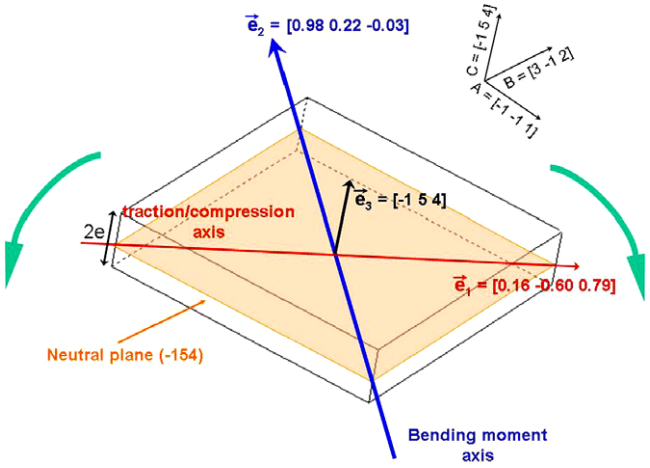

Fig. 6. Applied stress conditions producing bending straining at the scale of a single lath. A simplified, representative loading is applied to the simulation volume. The neutral plane coincides with the lath middle plane, normal to $\mathbf{e}_3 = [-154]$. The applied bending moment is parallel to direction $\mathbf{e}_2$ whereas the traction/compression axis is parallel to $\mathbf{e}_1$. The upper lath region (on top of the neutral plane) is loaded in traction while the lower lath region (below the neutral plane) is loaded in compression.

The stress applied to a given segment is determined using the following procedures:

1. The distance h of a particular segment with respect to the neutral plane is calculated, along the $\mathbf{e}_3$ direction. The sign of h depends on the position with respect to the neutral plane.
2. The local applied stress tensor is then given by Eq. (12) involving the reference tensile stress σ_{app}^{ref} along $\mathbf{e}_1$ acting in the upper lath.

In bending conditions as sketched in Fig. 6, one of the lath surfaces is loaded in tension while the other is loaded in compression, each surface bearing equal and opposite stresses. In these conditions, plastic strain generated at the scale of the whole simulation volume strictly cancels out: the plastic deformation in the upper lath region (above the neutral plane) is compensated by opposite plastic deformation (below the neutral plane). For this reason, an alternate variable is used to monitor the simulations: the curvature tensor $\underline{\underline{K}}$ derived from the Nye tensor.

The Nye tensor [27], noted $\underline{\underline{\alpha}}$, was developed to determine the closure mismatch of a linear path traced in a three-dimensional surface S enclosing a volume V, containing an arbitrary dislocation microstructure [28]. In the discrete edge/screw DD modelling, this tensor is computed by adding up the following infinitesimal contributions of every dislocation segment:

$$\alpha_{ij} = \frac{1}{V}\sum_{k=1}^{\mathrm{Nseg}} b_i^k t_j^k l^k, \tag{13}$$

where Nseg is the total number of segments in the volume V, b^k is the Burgers vector associated with the segment k, t^k is the unit vector aligned with the segment and l^k is the length of the segment k.

According to Eq. (13), any two dislocation populations of the same density and having opposite orientations $\mathbf{t}^{(i)}$ and $\mathbf{t}^{(j)}$ yield no net contribution to the tensor $\underline{\underline{\alpha}}$. Only the "geometrically necessary dislocations" (GNDs) [29,30] produce a net, non-vanishing contribution to Eq. (13).

The virtual segments, mentioned in Section 2.3, are of course excluded from the above summation. The tensor

α_{ij} is related to the lath curvature tensor K_{ij} by the following expression:

$$\alpha_{ij} = K_{ji} - K_{mm}\delta_{ij}, \tag{14}$$

where δ_{ij} are the components of the unity tensor and K_{mm} is the trace of tensor $\underline{\underline{K}}$. Therefore:

$$K_{ij} = \alpha_{ji} - \frac{1}{2}\alpha_{\mathrm{mm}}\delta_{ij}. \tag{15}$$

The tensor $\underline{\underline{K}}$ quantifies the plastic torsion and bending components imposed on the simulation volume. Diagonal terms K_{ii} represent the torsion about axis i, whereas non-diagonal terms K_{ij} correspond to the curvature of the volume V about direction i tangential to direction j.

In the simulations, bending conditions are imposed along K_{21} by using a feedback loop on the reference applied stress $\sigma_{\mathrm{app}}^{\mathrm{ref}}$.

At a given time step n, the reference stress magnitude $\sigma_{\mathrm{app}}^{\mathrm{ref}}$ (see Eq. (12)) depends on the difference between the rate and the imposed bending rate $\dot{K}_{21}^{\mathrm{imp}}$ computed over the last n_{aver} steps, as:

$$\sigma_{\mathrm{app}}^{\mathrm{ref}}(n) = \sigma_{\mathrm{app}}^{\mathrm{ref}}(n-1) - C[(K_{21}^{n} - K_{21}^{n-n_{\mathrm{aver}}}) - n_{\mathrm{aver}}\,\delta t\,\dot{K}_{21}^{\mathrm{imp}}]. \tag{16}$$

In the following simulations, a compliance factor $C = 5\ \mathrm{N\,m^{-1}}$ is used to tune the feedback corrections. The applied bending rate is $\dot{K}_{21}^{\mathrm{imp}} = 2\times10^{-9}\ \mathrm{m^{-1}\,s^{-1}}$ and $n_{aver} = 100$.

3. DD simulation results

In order to show the effect of temperature on the dislocation structures, simulations are performed at 50 and 200 K under the same constant imposed curvature rate $\dot{K}_{21}^{\mathrm{imp}} = 2\times10^{-9}\ \mathrm{m^{-1}\,s^{-1}}$. The results are compared alongside one another, for $K_{21} = 260$ and $522\ \mathrm{m^{-1}}$. The dislocation structures to be described in the following are representative of small plastic deformations. Indeed, the maximum plastic strain ε_{p} attained in a bent lath corresponds to half the lath thickness (in direction $\mathbf{e_3}$) times the plastic curvature [31]. At 200 K, the maximum plastic strain achieved here is thus $1\ \mu\mathrm{m} \times 520\ \mathrm{m^{-1}} = 5.2\times10^{-4}$.

3.1. Evolution of the dislocation densities

Below $K_{21} = 420\ \mathrm{m^{-1}}$, the total dislocation density ρ_{tot} obtained is slightly larger than at 50 K (about +10%, see Fig. 7a). Most of the dislocation segments are screws; the minimum proportion being about 18 screws for one edge (see Fig. 7b). The dislocation density ρ_{screw} thus evolves in the same manner as ρ_{tot}, since:

$$\rho_{\mathrm{screw}} = (\mathrm{r}\times\rho_{\mathrm{tot}})/(1+\mathrm{r}) \approx \rho_{\mathrm{tot}}, \tag{17}$$

where $r = \rho_{\mathrm{screw}}/\rho_{\mathrm{edge}} >> 1$. In the same fashion, the edge dislocation density ρ_{edge} is given by:

$$\rho_{\mathrm{edge}} = \rho_{\mathrm{tot}}/(1+r) \approx \rho_{\mathrm{tot}}/r. \tag{18}$$

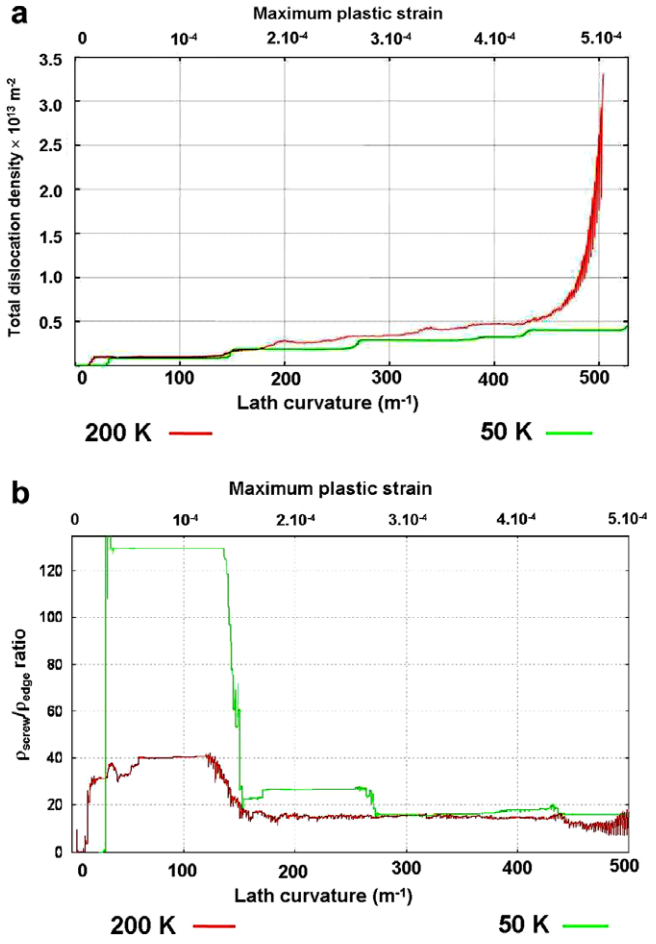

Fig. 7. DD simulation results: evolution of the dislocation densities. (a) Simulated total dislocation densities at 50 and 200 K. The total plastic strain in a bent lath strictly cancels out. ε_{p} indicated on the x-axis is the plastic strain in the lath outer surfaces, corresponding to the plastic curvature times half the lath thickness. (b) Dislocation density ratio, $\rho_{\mathrm{screw}}/\rho_{\mathrm{edge}}$, at 50 and 200 K.

According to Fig. 7b and using Eq. (18), it is readily seen that ρ_{edge} can have significant temperature dependence, depending on K_{21}. Such variations are obviously related to the screw dislocation mobility, coming from Eqs. (1) and (2). Indeed, for increasing temperature, faster screws generate longer accompanying edges segments per unit of time and the activation of secondary slip is stronger. No matter how small, the noted differences produce a significant effect on the mechanical response of the lath. Namely, the maximal applied stress[3] attains 320 MPa (at 200 K) instead of 420 MPa (at 50 K), under the same fixed plastic curvature rate conditions.

At 200 K, beyond $K_{21} = 420\ \mathrm{m^{-1}}$ (see Fig. 7a), a deformation regime characterized by a rapid increase in ρ_{tot} initiates. This regime is not an artefact due to the feedback control procedure. Rather, it coincides with very active cross-slip and subsequent formation of open-loop arrangements, as first described in Ref. [32] (see also Fig. 8b). Incidentally, open loops yield no net increase in the edge and screw dislo-

[3] The fixed plastic curvature rate is $2\times10^{-9}\mathrm{m^{-1}\,s^{-1}}$.

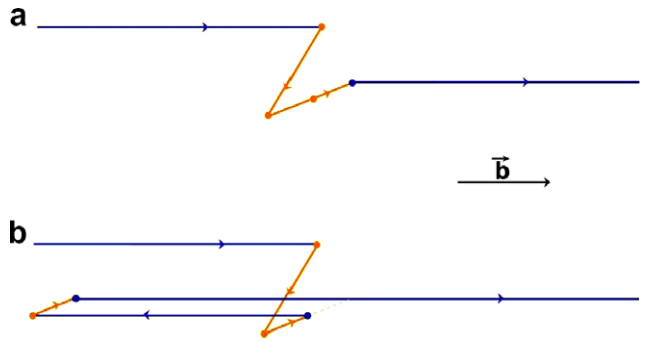

Fig. 8. Description and formation of open-loop configurations. (a). The edge portions gliding in opposite directions are immobilized, forming a cross-kink. (b) The point where the edges joined serves as a pinning point for one of the edge segments. New screw dislocations are generated very close to the initial ones, when a portion of one of the edges becomes mobile again.

cation lengths. According to Eq. (13), this means that the majority of the dislocations produced past $K_{21} = 420\ \mathrm{m}^{-1}$ are statistically stored dislocations. Hence, the rapid increase of ρ_{tot} visible in Fig. 7a has practically no effect on the plastic curvature (at 200 K) and the mechanical response past $K_{21} = 420\ \mathrm{m}^{-1}$.

3.2. Dislocation microstructure formation

The dislocation microstructures obtained at 50 K are presented in Fig. 9, for two different levels of plastic curvature. During the early deformation steps, the dislocation sources located in the virtual volume (where the applied stress magnitude is maximal) are activated and emit dislocations inside the lath, in the form of long screw segments. This movement leaves shorter, very mobile edge portions that soon pile-up in the $(-1\,-1\,1)$ and $(3\,-1\,2)$ oriented lath interfaces. These structures are located in zones ① and ② in Figs. 9 and 10. Unlike the edge segments, all the (early) screw segments have the same sign, and therefore contribute to the accumulation of plastic curvature.

In the lath zone loaded in tension, the MRSSP orientation falls in an anti-twin region (see Fig. 2): cross-slip is therefore inhibited in the tensile zone. In the lath zone loaded in compression, the MRSSP orientation falls in a twin region: cross-slip activity is concentrated in the compressive zone. Initially, the mobile screws keep on progressing in the lath until they arrive at the lath centre (neutral plane). No further glide takes place beyond that point, due to the reversal of the applied load polarity. Screw pile-ups are thus formed at the neutral plane (see Fig. 6) before new additional dislocations are emitted from the interfaces. Local stresses due to pile-ups [33] can contribute to activate isolated cross-slips events, including when little thermal activation is available. At 50 K, for example, the obtained open-loop arrangements are relatively small and sporadic, forming into well separate locations (see markers ③ in Figs. 9 and 10). Incidentally, very similar isolated structures are also found in 16MND5 steel, after deformation at 77 K [7,8] and were named "clusters". Activation of secondary slip is quite limited at 50 K, owing to the comparatively small shear stress acting in the $a/2[-1\,1\,-1](1\,1\,0)$ slip system (see Eq. (1)). Consequently, the activated secondary dislocations glide remain relatively close to the $(-1\,5\,4)$ lath interfaces, generating very short edge segments (see Fig. 9a and b).

At higher temperature (200 K), the early deformation stage is similar to that at low temperature (50 K). However, increased mobility of the screws and activation of secondary slip (compare Fig. 9a to Fig. 10a) generate longer accompanying edge segments, arrested in the $(-1\,-1\,1)$ and $(3\,-1\,2)$ lath interfaces (see markers ① and ②, in Figs. Figs. 9 and 10). This effect may explain why these (edge-type) arrangements are frequently found[4] in 16MND5 steel deformed at 273 K and not at 77 K [8]. Increased temperature also means stronger cross-slip activity in the lath region loaded in compression. Hence, relatively large zones containing numerous open loops are formed (see marker ③ in Fig. 10b). The local dislocation densities achieved in this way are very high (over $10^{15}\ \mathrm{m}^{-2}$). Therefore, in the absence of recovery due to cross-slip inhibition (see Fig. 2) and in the presence of obstacles (lath interfaces or neutral plane), the internal stress can locally exceed the applied stress. For this reason, the (local) MRSSP orientation can change and glide becomes possible in initially prohibited slip planes, inducing further densification of the microstructure. Beyond $K_{21} = 420\ \mathrm{m}^{-1}$, the dislocation densities tend to be asymmetric on either sides of the neutral plane, generating possible internal stress and strain incompatibilities. Further work is needed to analyze this effect.

Previous MD calculation results show that cross-kink unpinning can produce debris of various sizes, ranging from point defects to TEM-resolved dislocation loops (see Ref. [34] and Fig. 5b in Ref. [7]). Similar debris consisting of prismatic loops is found in the dislocation microstructures obtained by DD. However, the size of the debris has to be larger or equal to the lattice spacing used for the DD network (10 times the Burgers vector magnitude). The loops produced during the present simulations are mostly located in the high dislocation density region, and for this reason are not visible in the rather low-magnification views in Figs. 9 and 10. Note that the range of temperatures used for this study limits the production of debris, which is in good agreement with TEM observations [8]. Complementary studies perfomed with DD showed that the density of debris increases with the temperature, e.g when the screw velocity is closer to the edge velocity.

4. Summary and conclusions

Intra-lath plasticity is investigated using three-dimensional dislocation dynamics simulations specially adapted to treat 16MND5 steel deformation in the DBTT range. The edge segment velocity is proportional to the local effective resolved shear stress, whereas the screw dislocation mobility follows a thermal activation scheme. New cross-slip rules have been developed based on a kinetic Monte

[4] In Ref. [8] such structures are called "tilt boundaries".

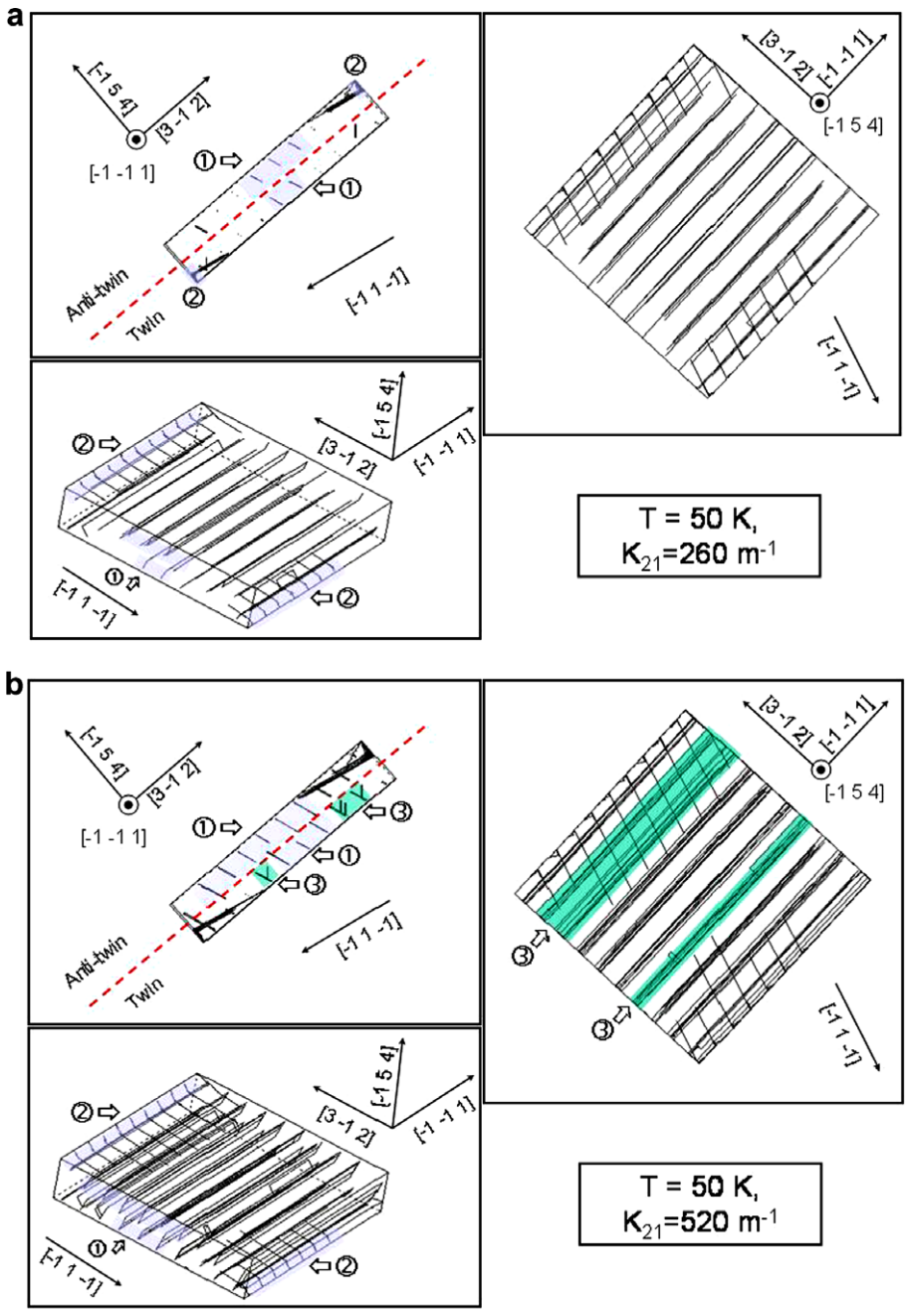

Fig. 9. Simulated dislocation microstructures obtained at 50 K and viewed from three different directions. (a) Low plastic curvature: 260 m^{-1}; (b) higher plastic curvature: 522 m^{-1}. The zones labelled ① correspond to edge dislocation arrays due to the $(-1-11)$ interfaces, whereas the zones labelled ② correspond to edge dislocation arrays due to the $(3-12)$ interfaces. The zones ③ correspond to high densities of open-loop arrangements, elongated in the $(-11-1)$ screw direction.

Carlo algorithm that account for the twinning/anti-twinning asymmetry. Specific applied loading and boundary conditions have been worked out, with a view to accounting for the bending deformation mode experimentally observed. The conclusions obtained using the presented DD simulations are summarized as follows:

1. During the early deformation steps, the initial mobile screw dislocations from the primary slip system pile-up close to the (-154) neutral plane. The accompanying edge segments generally increases in length with temperature and pile-up next to the $(-1-11)$ and $(3-12)$ lath interfaces. Unlike the edge segments, all screws have the same sign and contribute to the imposed plastic curvature.
2. In the lath zone loaded in compression, the orientation of the MRSSP is located in a twin region. The compressive zone thus concentrates most of the cross-slip activity. Beyond a curvature $K_{21} = 420\ m^{-1}$, the dislocation density tends to be asymmetric between the two sides

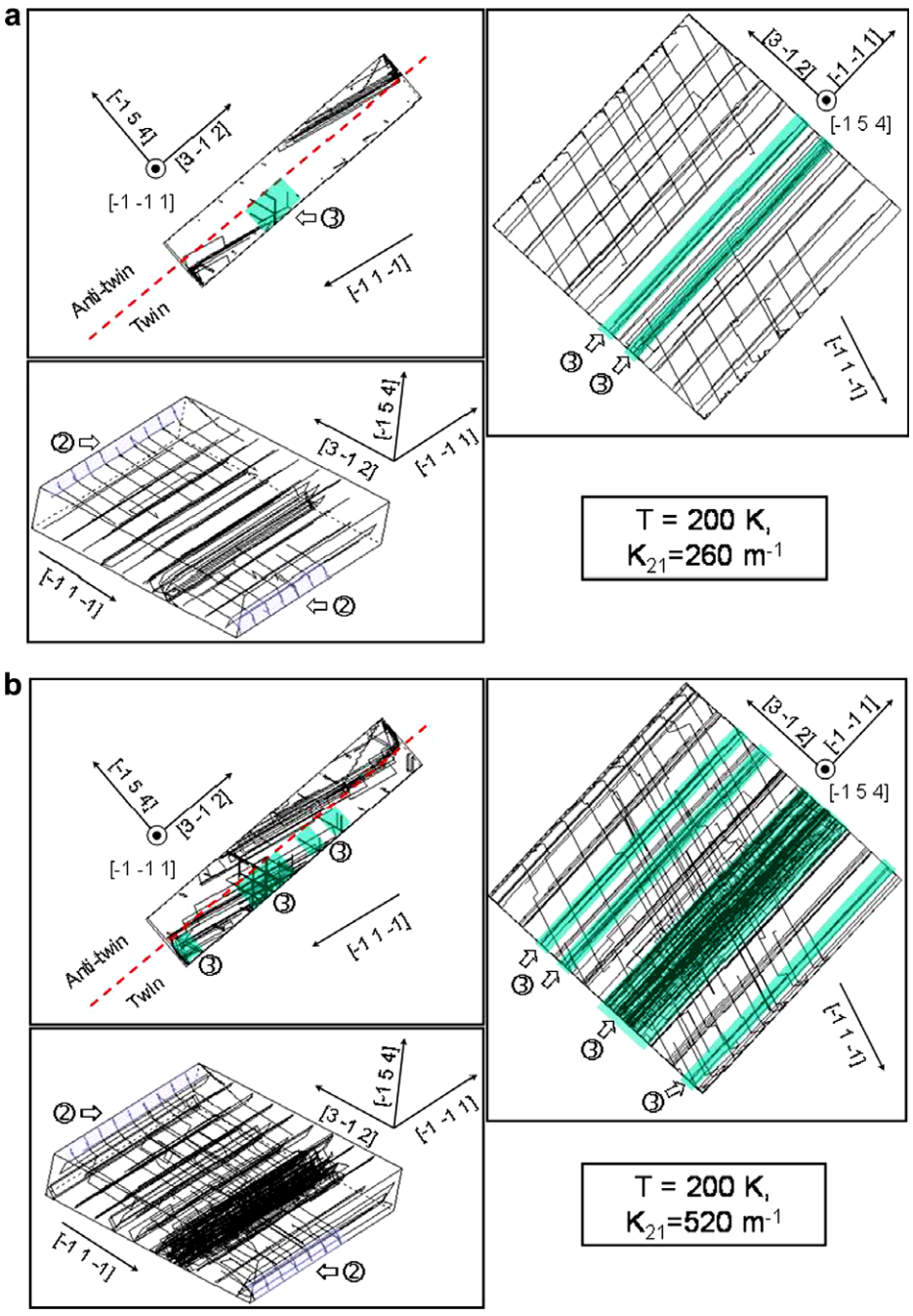

Fig. 10. Simulated dislocation microstructures obtained at 200 K and viewed from three different directions. (a) Low plastic curvature: 260 m^{-1}; (b) higher plastic curvature: 522 m^{-1}. Note the pronounced dislocation density asymmetry across the neutral plane (represented by a dashed line). The zones labelled ① correspond to edge dislocation arrays due to the $(-1\,-1\,1)$ interfaces, whereas the zones labelled ② correspond to edge dislocation arrays due to the $(3\,-1\,2)$ interfaces. The zones ③ correspond to high densities of open-loop arrangements, elongated in the $(-1\,1\,-1)$ screw direction.

of the neutral plane, generating possible intra-lath stress and strain incompatibilities.

3. Below a curvature $K_{21} = 420\ m^{-1}$, the screw dislocation density obtained at 200 K is only slightly larger than at 50 K (+10%). No matter how small, this difference is associated with a significant effect on the mechanical response of the lath (+36% maximal applied stress).
4. The implemented cross-slip behaviour plays an essential role in the development of specific dislocation arrangements, associated with the production of open-loop arrangements. At 50 K, such arrangements are formed sporadically, and with the help of internal stresses. At 200 K, especially beyond $K_{21} = 420\ m^{-1}$, the same process is much more frequent and produces relatively large, high-density structures.
5. The dislocation structures generated in DD explain the features observed in actual 16MND5 steels after tensile deformation and/or brittle fracture, in spite of the relatively limited plastic strain achieved during the simulations. Thus, further analysis of the numerical results

can provide insight into the deformation mechanisms possibly involved during cleavage initiation and propagation.

References

[1] Carassou S. Doctoral thesis, Ecole des Mines de Paris, SRMA/CEA/Saclay; 1999.
[2] Carassou S, Renevey S, Marini B, Pineau A. ECF12 Proceedings, Sheffield 1998;2:691.
[3] Reveney S. Doctoral thesis, Université Paris XI Orsay, SRMA/CEA/Saclay; 1998.
[4] Karlik M, Nedbal I, Siegl J. Mater Sci Eng A 2003;357:423.
[5] Bain EC. Metall Mater Trans B 1972;3(5):1031.
[6] Bhadeshia HKDH. Bainite in steels. Institute of Materials, Minerals and Mining 2001.
[7] Obrtlik K, Robertson CF, Marini B. J Nucl Mater 2005;342:35.
[8] Robertson CF, Obrtlik K, Marini B. J Nucl Mater 2007;366:58.
[9] Bulatov VV, Cai W. In: Sutton AP, Rudd RE, editors. Computer simulations of dislocations. Oxford: Oxford University Press; 2006.
[10] Weygand D, Friedman LH, Van der Giessen E, Needleman A. Mater Sci Eng A 2001;309–310:420.
[11] Cleveringa HHM, Van der Giessen E, Needleman A. Int J Plast 1999;15:837.
[12] Yefimov S, Van der Giessen E, Groma I. Modell Simul Mater Sci Eng 2004;12:1069.
[13] Tang M, Kubin LP, Canova GR. Acta Mater 1998;46:3221.
[14] Tang M, Devincre B, Kubin LP. Modell Simul Mater Sci Eng 1999;7:893.
[15] Caillard D, Martin JL. Thermally activated mechanisms in crystal plasticity. Oxford: Pergamon Press; 2003.
[16] Verdier M, Fivel M, Groma I. Modell Simul Mater Sci Eng 1998;6:755.
[17] Kocks UF, Argon AS, Ashby MF. Prog Mater Sci 1975;19:1.
[18] Libert M. Doctoral thesis, Ecole Centrale de Paris, SRMA/CEA/Saclay; 2007.
[19] Chaussidon J, Fivel M, Rodney D. Acta Mater 2006;54:3407.
[20] Domain C, Monnet G. Phys Rev Let 2005;95:215506.
[21] Christian JW. Metall Trans A 1983;14A:1237.
[22] Vitek V, Mrovec M, Bassani JL. Mater Sci Eng A 2004;365:31.
[23] Vitek V, Mrovec M, Gröger R, Bassani JL, Racherla V, Yin L. Mater Sci Eng A 2004;387–389:138.
[24] Sekfali S. Doctoral thesis, Ecole Centrale de Paris, LMSSMat/SRMA/CEA/Saclay; 2003.
[25] Halegaar JHA, Bitzek E, Flipse CFJ, Gumbsch P. Phys Rev B 2006;73:045425.
[26] Bouaziz O, Maugis P, Embury JD. Scripta Mater 2006;54:1527.
[27] Nye JF. Acta Metall 1953;1:153.
[28] Sun S, Adams BL, King WE. Phil Mag A 2000;80(1):9.
[29] Fivel M, Forest S. Techniques de l'ingénieur, 2004; MB1 noM4016:M4016.1.
[30] Ashby MF. Phil Mag 1970;21:399.
[31] Timoshenko SP, Goodier JN. Theory of elasticity. 3rd ed. New York: McGraw-Hill; 1970.
[32] Louchet F, Saka H. Mater Sci Eng A 2003;352:71.
[33] Déprés C, Robertson CF, Fivel MC. Phil Mag A 2004;84:2257.
[34] Marian J, Cai W, Bulatov V. Nat Mater 2004;3:158.